Light atom quantum oscillations in UC and US

Yuen Yiu,[1,*] A. A. Aczel,[2,†] G. E. Granroth,[3] D. L. Abernathy,[2] M. B. Stone,[2] W. J. L. Buyers,[4] J. Y. Y. Lin,[5]
G. D. Samolyuk,[6] G. M. Stocks,[6] and S. E. Nagler[2]
[1]*Department of Physics and Astronomy, University of Tennessee, Knoxville, Tennessee 37996, USA*
[2]*Quantum Condensed Matter Division, Oak Ridge National Laboratory, Oak Ridge, Tennessee 37831, USA*
[3]*Neutron Data Analysis and Visualization Division, Oak Ridge National Laboratory, Oak Ridge, Tennessee 37831, USA*
[4]*Canadian Neutron Beam Centre, Canadian Nuclear Laboratories, Chalk River, Ontario, Canada, K0J 1J0*
[5]*California Institute of Technology, Pasadena, California 91125, USA*
[6]*Materials Science and Technology Division, Oak Ridge National Laboratory, Oak Ridge, Tennessee 37831, USA*

(Received 6 August 2015; revised manuscript received 18 December 2015; published 19 January 2016)

High-energy vibrational scattering in the binary systems UC and US is measured using time-of-flight inelastic neutron scattering. A clear set of well-defined peaks equally separated in energy is observed in UC, corresponding to harmonic oscillations of the light C atoms in a cage of heavy U atoms. The scattering is much weaker in US and only a few oscillator peaks are visible. We show how the difference between the materials can be understood by considering the neutron scattering lengths and masses of the lighter atoms. Monte Carlo ray tracing is used to simulate the scattering, with near quantitative agreement with the data in UC, and some differences with US. The possibility of observing anharmonicity and anisotropy in the potentials of the light atoms is investigated in UC. Overall, the observed data is well accounted for by considering each light atom as a single atom isotropic quantum harmonic oscillator.

DOI: 10.1103/PhysRevB.93.014306

I. INTRODUCTION

The complex electronic structure of uranium leads to a wide variety of unusual and diverse behaviors in the uranium salts U*X* (*X* = C, N, P, S, As, Se, Sb, Te, and Bi), and therefore the materials in this family have been the subject of many past investigations characterizing their magnetic and vibrational properties [1–12].

Despite this effort, many unresolved issues remain, including the origin of unusual magnetic excitation spectra in several of the materials [8,9], including antiferromagnetic UN ($T_N =$ 53 K [13]) and ferromagnetic US ($T_c = 180$ K [14]). Indeed, our original motivation to study these materials using time-of-flight neutron scattering methods was to closely examine the high-energy portion of the magnetic excitation spectra. This required a careful study of the vibrational scattering at these energies as well. Moreover, there has been renewed interest in more detailed calculations of the vibrational properties of this family as certain members, including UN and UC, are under active consideration for next generation nuclear fuels [15–17].

The recent neutron scattering studies of UN resulted in the discovery of new and unexpected features in the vibrational spectrum [18]. The same single crystal of UN investigated in earlier work [8,10,19] was reexamined via modern neutron time-of-flight (TOF) spectroscopy using the SEQUOIA [20,21] and ARCS [22] spectrometers at the Spallation Neutron Source, Oak Ridge National Laboratory. Specifically, strong vibrational scattering was found at energies above the usual acoustic and optic phonon branches. A series of evenly-spaced, high-energy modes was observed, and detailed quantitative analysis showed that these modes could be attributed to the nitrogen atoms behaving as independent, isotropic, 3D quantum harmonic oscillators (QHOs) [18,23]. Some of the features of the QHO modes, for example, the intrinsic broadening, were consistent with predictions of a binary solid model [24]. This model applies to systems with two different types of atoms with disparate masses and explains how the motion of the heavy atoms affects the QHO behavior of the lighter ones.

The observation of these well defined modes at energies above the highest optic phonon branches in an ordered single-crystal contrasts with the conventional view of the vibrational response in crystalline solids. In this regime, the vibrational response is usually weak and relatively featureless [25]. Prior to the UN discovery, exceptions to this rule were generally found in binary metallic hydrides [26–30], for example, in ZrH_x systems, where hydrogen atoms occupy interstitial sites [28]. However, in those systems, the hydrogen modes usually exhibit significant anisotropic and anharmonic effects, mainly due to H-H interactions, crystalline anisotropy, and the diffusion of the H atoms [26–29]. Typically, only a few modes are observed. Conversely, the nitrogen oscillations in UN show well-defined peaks up to the 10th order.

Known prerequisite conditions for the QHO modes to be clearly observable in binary alloys include a large mass ratio between the light and heavy atoms, and weak interactions between light atoms. Although the aforementioned binary solid model provides some guidance, there is little experimental information on the dependence of this part of the vibrational response function on factors such as the mass ratio and atomic neutron cross-sections. In this work, we investigate how these factors affect the high-energy vibrational scattering in UX via time-of-flight neutron spectroscopy measurements on single crystals of UC and US. For UC, we find a series of well-defined high-energy vibrational modes analogous to those observed for UN. Overall these modes are described well by a QHO model for the carbon atoms. Conversely, while the US data also show evidence for the high-energy vibrational modes,

---

[*] yyiu@vols.utk.edu

[†] aczelaa@ornl.gov

only the lowest few are observed and they are much weaker in intensity compared to those seen in UC and UN. We discuss the reasons for these differences. In addition, we explore the effect of multiple scattering on the observed spectrum, and the possibility of extracting information on the directional dependence and anharmonicity of the light atom potential via measurements of the QHO modes.

II. INELASTIC NEUTRON SCATTERING

All neutron scattering measurements reported here were collected using the SEQUOIA [20,21] and ARCS [22] TOF Fermi chopper spectrometers at the Spallation Neutron Source of Oak Ridge National Laboratory. The same depleted uranium single crystals of UC and US used in previous studies were investigated in this work [31,32]. Both samples had similar total volumes on the order of 1 cm^3. For the neutron scattering experiments, each single crystal was mounted in an aluminum can and loaded in a closed cycle helium refrigerator. All data were collected at $T = 4$ K, with the $[HHL]$ scattering plane horizontal. A Fermi chopper was used to obtain several different incident neutron energies, including $E_i = 80$, 250, 500, 700, and 800 meV. The details for each chopper setting are given in Table I. All data sets were normalized against a vanadium standard to account for variations of the detector response and the solid angle coverage.

Empty-can measurements were performed at $T = 4$ K and subtracted from the US data sets. A small amount of Al from the sample mount was not perfectly accounted for in the US empty-can measurement; we discuss below the implications of this imperfect background subtraction on the scattering observed in US. On the other hand, the fragility of the UC crystal required a unique sample mounting arrangement that could not be disassembled and therefore prevented a comparable empty can measurement. It is well known that Al scattering is strongest at low energies up to the cutoff in the Al phonon density of states. Furthermore, when high incident neutron energies are chosen (i.e., 500 meV), the overall scattering from Al also includes a significant multiphonon contribution and over most of the measured energy transfer range the intensity decays approximately exponentially with energy. Due to the lack of an appropriate Al empty can subtraction for UC, Al single phonon and multiphonon effects are directly included in the UC simulations, as discussed below.

TABLE I. List of experimental conditions used to collect data for (a) UC and (b) US, on SEQUOIA ($E_i = 80$ meV only) and ARCS ($E_i = 80$, 250, 500, 700, and 800 meV). Here, d_{FC} is the slit spacing of the Fermi chopper, R_{FC} is the radius of curvature of the Fermi chopper, ν_{FC} is the frequency of the Fermi chopper, ν_{T0} is the frequency of the T0 chopper, and ΔE FWHM represents the corresponding instrumental energy resolution at zero energy transfer.

	(a) UC, $T = 4$ K			
E_i (meV)	80	500	700	800
d_{FC} (mm)	1.5	0.5	0.5	0.5
R_{FC} (m)	0.58	1.53	1.53	1.53
ν_{FC} (Hz)	120	480	600	600
ν_{T0} (Hz)	90	180	180	180
ΔE FWHM (meV)	9.0	18.2	26.1	31.4
	(b) US, $T = 4$ K			
E_i (meV)	80	250	500	
d_{FC} (mm)	3.6	0.5	0.5	
R_{FC} (m)	1.53	1.53	1.53	
ν_{FC} (Hz)	240	360	480	
ν_{T0} (Hz)	90	180	180	
ΔE FWHM (meV)	4.1	8.8	18.2	

Figure 1 shows representative measurements with $E_i = 80$ meV for (a) UC from ARCS and (b) US from SEQUOIA along the $[\bar{2}\bar{2}L]$ direction in reciprocal space. The results for the acoustic and optic phonons are consistent with those previously reported in the literature [10,31]. Both the acoustic and optic modes in nonmagnetic UC are clearly visible with large signal compared to background. On the other hand, the phonon modes of US are only weakly visible in the data. We note also that weak magnetic scattering is present near the ferromagnetic zone center $(\bar{2}\bar{2}0)$ extending up to at least 60 meV.

The decreased intensity of the phonon scattering in US can be understood by considering the one phonon structure factor, g, for the rocksalt structure. Along symmetry directions this

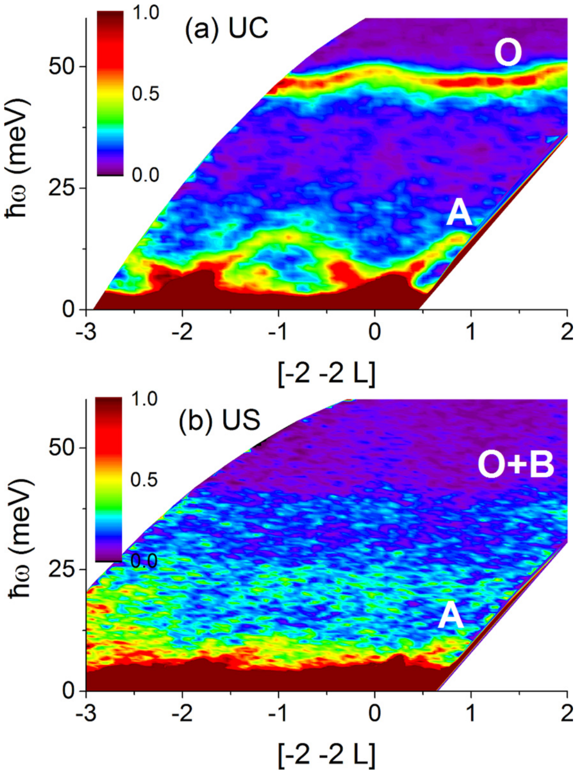

FIG. 1. The phonons along the $[\bar{2}\bar{2}L]$ direction for (a) UC (ARCS) and (b) US (SEQUOIA) with $E_i = 80$ meV. In both cases, the acoustic and optic phonon modes are well separated. The optic modes' signal to background ratio is much higher for UC as compared to US. The energies of the optic modes for UC and US are known to be 48 and 40 meV [10]. The white text O and A indicate the general location for the optic and acoustic phonon modes, while B denotes significant background contribution. As mentioned in the text, additional scattering is observed in the US plot centered about the ferromagnetic zone center $(\bar{2}\bar{2}0)$; this scattering is visible most clearly between 40 and 60 meV.

TABLE II. Relevant parameters for phonon intensities in UC, UN, US, and Al [34].

Atom	m (amu)	b (fm)	b^2/m (fm^2/amu)
N	14	9.4	6.31
C	12	6.6	3.63
S	32	2.8	0.25
U	238	8.4	...
Al	27	3.4	...

can be written as [3,33]

$$g^2 = (\mathbf{Q}\cdot\boldsymbol{\xi})^2 g'^2 \tag{1}$$

with

$$g' = \left(\frac{b_U e_U}{\sqrt{M}} \pm \frac{b_X e_X}{\sqrt{m}}\right), \tag{2}$$

where $\mathbf{Q}$ is the neutron momentum transfer, $\boldsymbol{\xi}$ is a unit vector describing the phonon polarization, M is the mass of U, m is the mass of the light atom X, e_U and e_X are the eigenvectors of the U and the X ions, subject to the constraint $e_U^2 + e_X^2 = 1$, and b_U and b_X are the coherent neutron scattering lengths [3]. The sign between the two terms in Eq. (2) depends on the (HKL) indices of the Brillouin zone, where $(+)$ and $(-)$ correspond to all even and all odd indices respectively.

For optic phonons, at the zone center, $|e_U^2 M| = |e_X^2 m|$ and therefore g' can be rewritten as

$$g' = b_U\sqrt{\frac{m}{M(M+m)}} \pm b_X\sqrt{\frac{M}{m(M+m)}}. \tag{3}$$

In the limit of $M \to \infty$,

$$\lim_{M\to\infty} g'^2 = \frac{b_X^2}{m} \tag{4}$$

This expression indicates that the intensity of the optic modes is determined primarily by the mass and scattering length of the light atoms. Under the assumption of similar scattering lengths, the intensity of the optic modes decreases with increasing mass m of the light atom. Table II further emphasizes this point by comparing several parameters relevant to the phonon intensities of UC, UN, and US [34]. It is seen that the optic phonon cross section for US is more than an order of magnitude smaller than the comparable cross-sections for UC or UN. Al is also included in the table since it leads to significant background scattering in the US experiments, as discussed below.

Figure 2 depicts the orientationally averaged, high-energy response observed for both UC and US on ARCS. Several evenly-spaced vibrational modes are easily visible in the UC $E_i = 500$ meV spectrum shown in Fig. 2(a). In the US data with $E_i = 500$ meV shown in Fig. 2(b), ferromagnetic fluctuations are seen at low Q, but the high-energy vibrational modes are barely visible. On the other hand, some weak vibrational modes can be ascertained in the higher resolution $E_i = 250$ meV data depicted in Fig. 2(c). In both materials, the vibrational modes appear on inspection to be evenly spaced.

We first discuss the vibrational scattering seen in UC. Figure 3 shows the $E_i = 500$ meV Q-integrated data for UC, with two different panels corresponding to linear (top) and logarithmic (bottom) y axes. Modes up to seventh order are clearly visible as peaks in the data. To test whether these are evenly spaced, the Q-integrated data set is fitted to the following functional form:

$$I(E) = \sum_n T_n e^{-\frac{(E-E_n)^2}{2\sigma_n^2}} + B_{\exp} e^{-\lambda_B E} + B_0. \tag{5}$$

T_n is a scale factor for each individual Gaussian peak and σ_n is the standard deviation for each peak. An empirical background consisting of a constant B_0 and decaying exponential $B_{\exp} e^{-\lambda_B E}$ was incorporated into the fit. The decaying exponential term is expected from a simple diffusive model of multiphonon scattering [35,36]. E_n are the mode positions that were fit independently and the last term incorporates all others sources of background.

The solid line in Fig. 3 represents the fitted curve from Eq. (5). The fitted peak positions of the modes for all measured data sets are shown in Table III, and are evenly spaced. The average spacing between the modes, incorporating all fitted data sets, was found to be $\hbar\omega_0 = 48 \pm 1$ meV for UC. The values are averaged by a weighted approach meaning $\hbar\omega_0 = (\hbar\omega_1 + \hbar\omega_2/2 + \hbar\omega_3/3 + \cdots + \hbar\omega_n/n)$. Values calculated from individual peaks, i.e., $\hbar\omega_n/n$ deviate from the

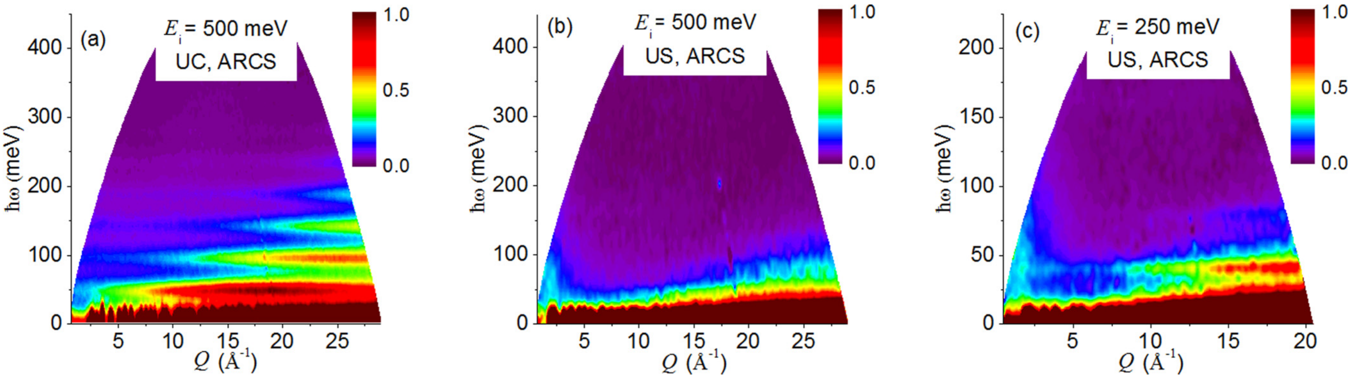

FIG. 2. Color contour plots of the inelastic neutron scattering spectra for (a) UC, $E_i = 500$ meV, (b) US, $E_i = 500$ meV and (c) US, $E_i = 250$ meV. The evenly-spaced, high-energy vibrational modes are clearly visible in the UC plot, but much less pronounced in the case of US. The low-Q inelastic scattering seen for US arises from ferromagnetic fluctuations.

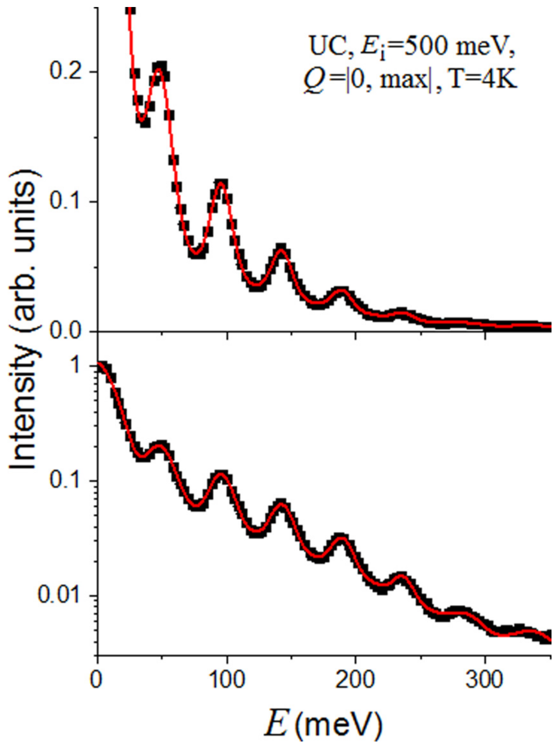

FIG. 3. The Q-integrated intensity vs energy plot for UC at 4 K, with $E_i = 500$ meV. The upper plot shows the systematic decline of intensity for higher modes. The lower (log) plot shows that the QHO modes remain visible for this data set up to the seventh mode. The black points are from the experimental data and the solid red line is the fit to the data using Eq. (5).

average by less than 1 meV, which implies a highly harmonic potential.

The fact that the spectrum is characterized by a series of evenly-spaced modes suggests that the light atoms behave like independent 3D QHOs similar to UN [18]. This hypothesis can be tested quantitatively by comparing the relative intensities of the modes to the known dynamical structure factor for the nth mode of a QHO at low T, which has a simple analytical form given by

$$S_n(Q,\omega) = \frac{D}{n!}\left(\frac{\hbar Q^2}{2m\omega_0}\right)^n exp\left(\frac{-\hbar Q^2}{2m\omega_0}\right)\mathcal{F}_n(\omega), \tag{6}$$

where $\mathcal{F}_n(\omega) = \delta(\hbar\omega - n\hbar\omega_0)$ and D is a constant.

TABLE III. Peak positions of the high-energy vibrational modes (in meV) for UC from fits to the Q-integrated data. Note that the error bars are statistical from the fitting of the data and do not account for instrumental resolution or systematic effects.

(a) UC, $T = 4$ K

$n\backslash E_i$	500 meV	700 meV	800 meV
1	47.7(3)	. . .	. . .
2	96.2(3)	98.1(2)	99.7(4)
3	142.8(4)	144.1(3)	146.0(5)
4	189.1(6)	190.9(3)	193.0(4)
5	235.6(1)	237.3(4)	239.0(4)
6	283.8(36)	283.7(6)	284.7(6)
7	. . .	329.9(7)	331.0(1.0)
8	. . .	372.9(1.2)	375.5(1.7)

average $\hbar\omega_0$: 48 ± 1 meV.

Assuming that one has a carbon atom QHO with the measured energy spacing of $\hbar\omega_0 = 48$ meV and a mass of 12.01 *amu* the calculated value of $\hbar/2m\omega_0$ is 0.0036 Å^2. Given the range of Q measured and the Q dependence in Eq. (6), it is surprising that the higher-order modes are visible in Fig. 2. This can be understood by considering that $S_n(Q,\omega)$ only accounts for single scattering events. With equally spaced modes, however, the contributions from multiple scattering will also peak at energies corresponding to QHO mode positions, and as discussed below the multiple scattering contributes to the intensity at low Q.

We consider the meaning of a single scattering event in both QHO language and an alternate, but equivalent description based on creating Einstein phonons of fixed frequency. At $T = 0$, an inelastic neutron scattering event, at an energy of $n\hbar\omega_0$ in QHO language, represents a transition from the QHO ground state to the nth eigenstate. In Einstein mode language, it consists of a single scattering event, with total wave-vector transfer magnitude Q, that creates n Einstein phonons, each of energy $\hbar\omega_0$. In either case, the scattering cross-section contains a factor Q^{2n}. On the other hand, a multiple scattering event in QHO language corresponds to a set of multiple transitions from the ground state to the nth excited state, while in the phonon description several different scatterings occur creating in aggregate n Einstein phonons. The jth scattering event contributes a factor Q_j^2 to the total observed cross-section. These processes are depicted in Fig. 4 for the case $n = 2$. The single scattering event shown in Fig. 4(a) will have an intensity $I \sim Q^4$ and a requirement that the vector sum of the individual Einstein phonon momenta $\mathbf{Q_1}$ and $\mathbf{Q_2}$ has a magnitude equal to Q. On the other hand, in the multiple scattering event shown in Fig. 4(b) each created Einstein phonon contributes a separate factor to the measured intensity, which is, therefore, proportional to $(Q_1Q_2)^2$. The total net

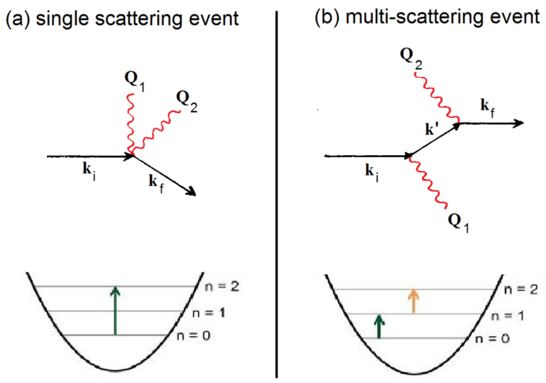

FIG. 4. Schematics showing the difference between (a) single scattering processes and (b) multiple scattering processes leading to the observed neutron scattering spectra for UC, UN, and US. k_i and k_f refer to the incident and final neutron momenta. In (b), values of $\mathbf{Q_1}$ and $\mathbf{Q_2}$ were chosen such that the total momentum transfer $\mathbf{Q} = 0$ but the scattering intensity is nonzero (see text for details).

vector momentum transfer $\mathbf{Q}$ measured in the experiment can take on a wide range of values, including $\mathbf{Q} = 0$ as depicted in the figure. The average over all possible multiple scattering combinations can lead to a cross-section that is independent of Q. Therefore the observed intensity of the higher-order peaks at small Q arises principally from multiple scattering.

With this in mind, we fit the constant-E cuts of the UC data to a modified expression of $S(Q,\omega)$ for QHOs [18], given by

$$S_n(Q,\omega) = A_n Q^{2n} \exp(-CQ^2) + B_n. \qquad (7)$$

Here, C is $\hbar/2m\omega_0$ and a Q-independent B_n term is included to account for the multiple scattering described above. For the ideal QHO model, $A_n/D = C^n/n!$. By relaxing this constraint and allowing A_n and C to be independent parameters in the data fitting, one can gain a sense of how much the UC data deviates from the ideal QHO limit.

Figure 5(a) depicts constant-E cuts from the 500 meV data set for the $n = 1$–5 modes, centered about $n\hbar\omega_0$ for the nth mode (20-meV integration range). Similar cuts were made for the $E_i = 700$ and 800 meV data sets (not shown). Figure 5(b) plots the ratios of the fitted parameters A_n/A_1 for the $E_i = 500$, 700, and 800 meV data sets. The solid line indicates the prediction for the QHO model with $\hbar\omega_0 = 48$ meV, with the noninteger n values interpolated by using $\Gamma(n+1)$ to calculate $n!$. As in the case of UN, there is excellent agreement between the QHO model and the data over 20 orders of magnitude. The experimental C value, corresponding to the zero point motion of the oscillator, also agrees well with the model. By incorporating all three data sets into the fit, the average value of C was found to be 0.0031(1) Å^2, which is close to the calculated value for the ideal QHO of 0.0036 Å^2 discussed above. These findings provide strong confirmation that the high-energy vibrational modes observed in UC correspond to quantum oscillations of the carbon atoms in the system.

Figure 6 shows the Q-integrated data for US with $E_i = 250$ and 500 meV, including fitted curves using Eq. (5). The same fitting approach, described earlier for UC, was also used for the US data. However, due to the weaker mode intensities in US, it is not possible to fit as many peaks in the US data sets. Nonetheless the modes are evenly spaced, similar to UC, with an average $\hbar\omega_0$ of 41(1) meV. The fitted peak position of each individual mode is shown in Table IV.

The weak intensities of higher QHO modes in US can be largely explained by the phonon structure factor of the rocksalt structure, as discussed earlier by Eqs. (3) and (4) and Table II. The greater mass and shorter scattering length of

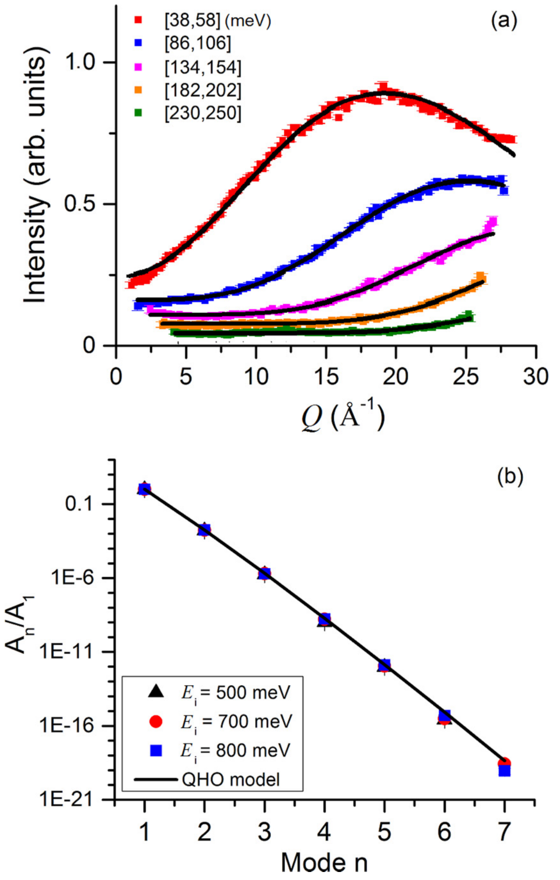

FIG. 5. (a) The Q dependence of the intensity for the $n = 1$–5 UC oscillator modes with $E_i = 500$ meV, integrated over the energy ranges shown in the legend. The solid lines are fits to the QHO model described in the text. (b) The A_n coefficients for the $n = 1$–5 modes normalized by the values of A_1. The coefficients are extracted from fits to the $E_i = 500$ (black triangles), 700 (red circles), and 800 meV (blue squares) ARCS data sets. The solid line is the prediction of the QHO model with $\hbar\omega_0 = 48$ meV and m corresponding to the mass of a carbon atom. The ratio is plotted on a logarithmic scale and spans almost 20 orders of magnitude.

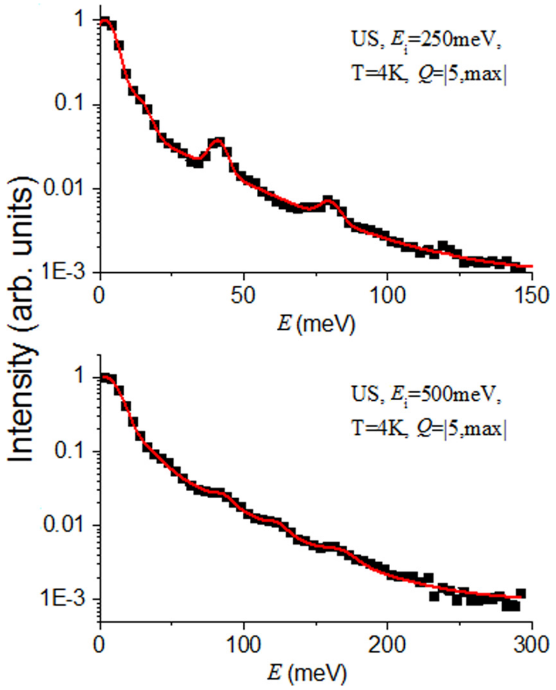

FIG. 6. The Q-integrated intensity vs energy plot for US at 4 K, with $E_i = 250$ and 500 meV. The QHO modes are much less intense compared to those observed in UC, with only three modes observable for $E_i = 250$ meV and four for $E_i = 500$ meV. The black points are from the experimental data and the solid red lines are the fits to the data using Eq. (5). Note that the Q-integrated range for the US data is $Q > 5$ Å^{-1} only. This is done to avoid contributions from the magnetic excitations at low Q as seen in Figs. 2(b) and 2(c).

TABLE IV. Peak positions of the high-energy vibrational modes (in meV) for US from fits to the Q-integrated data. Note that the error bars listed are from the fitting of the data and do not account for instrumental resolution.

	US, $T = 4$ K	
$n\backslash E_i$	250 meV	500 meV
1	40.9(3)	...
2	79.9(9)	85.6(2.4)
3	...	122.9(3.6)
4	...	166.7(5.8)
	average $\hbar\omega_0$: 41 ± 1 meV	

sulfur results in a much smaller b^2/m compared to carbon or nitrogen. At small Q, the scattering at the nth mode position is dominated by multiple scattering processes sequentially creating single optic phonons. The observed cross-section is therefore proportional to $(b^2/m)^n$. For this reason, the higher QHO modes appear much weaker in US compared to UC.

The correction for the Al background scattering is also a significant complication for the observation of QHO modes in US. The QHO cross-section for each mode reaches a maximum at the value of Q where the mode energy corresponds to the energy of the recoil scattering, which is given for an atom of mass m by $E_{\text{recoil}} = \hbar^2 Q^2/2m$. As seen in Table II, the masses of Al and S are relatively close, so the recoil scattering from the Al is strong near the position where one expects to observe the most intense QHO scattering from S. Altogether, quantitative analysis of the intensity of the QHO modes in US is more difficult.

III. MONTE CARLO RAY TRACING SIMULATIONS

Monte Carlo (MC) ray tracing simulations of both the UC and US ARCS neutron scattering experiments were performed to gain a better understanding of the various factors contributing to the observed scattering intensity. This approach worked exceptionally well to describe the neutron scattering spectra observed for UN [23]. The ability to model more realistic instrument and sample configurations is ever increasing [37,38]. The simulations took advantage of the hierarchical representation of neutron components and samples made possible in the MC ray tracing program Monte Carlo Virtual Neutron Experiment (MCViNE), which was developed in the Distributed Data Analysis for Neutron Scattering Experiments (DANSE) software development project [39]. The MCViNE simulations of neutron beams in these instruments were derived from corresponding McStas simulations [20,40–43].

In each simulation, the sample was modeled as a cube with a 1 cm^3 volume, approximating the shape of the sample used in the measurement. The configuration files for the simulations were created through a series of simple modifications to the files used for the UN MC simulations described in detail in Ref. [23], allowing for a straightforward extension of those calculations to UC and US.

Intrinsic broadening of the QHO modes is included in the simulation, as it is observed experimentally and predicted by the binary solid model [24]. The broadening arises from the fact that the heavy U atoms are not completely stationary, and can be modeled by replacing the Dirac-Delta function in the QHO expression with a Gaussian:

$$\mathcal{F}(\omega) = \exp\left(-\frac{(\hbar\omega - n\hbar\omega_o)^2}{2\Gamma^2(T)}\right), \tag{8}$$

where the Gaussian width $\Gamma(T)$ is a function of temperature and given by

$$\Gamma^2(T) = \frac{\hbar^2 Q^2}{2M}\int_0^{\theta} du\, Z(u) u \coth\left(\frac{\hbar u}{2k_B T}\right). \tag{9}$$

Here, M is the mass of the heavy atom, in this case the U atom. $Z(u)$ is the acoustic phonon density of states calculated with a Born-Van Karmen model and θ is the maximum band frequency for the acoustic phonon modes.

A Monte Carlo ray tracing simulation for UC with $E_i =$ 500 meV is shown as a color contour plot in Fig. 7(a) and the Q-integrated result is presented in Fig. 7(d). This simulation is similar to the one reported in Ref. [23] for UN and includes various sample kernels accounting for elastic scattering, QHO scattering (from carbon atoms), acoustic phonon scattering (single and multiphonon), and all forms of multiple scattering arising from the processes described above. As discussed earlier, the multiphonon contribution from the optic phonons is equivalent to QHO scattering. Multiphonon processes simultaneously involving both the acoustic and optic phonons lead to the intrinsic broadening accounted for by Eqs. (8) and (9) and are thus also included in the simulation.

Recall that the Al empty can scattering was not subtracted from the UC data. Figure 7(d) also shows a simulation with an additional term approximating the Al contribution as a disk with a total mass similar to the Al sample assembly used in the UC experiment. This significantly improves the agreement of the UC simulation with the data at energy transfers below 100 meV. The fractional contribution of Al to the total scattering can be estimated from the difference between the curves with and without the Al background term. At low energy transfers, the contribution of Al scattering to the background at the local minima between the QHO peak positions can be substantial, as high as 30% of the total signal. However, at an energy transfer of 150 meV, the fraction of the total scattering from Al is approximately 1%, and this drops off strongly as the energy transfer increases.

Monte Carlo simulations for US, incorporating sample kernels with the same ingredients as for UC, are shown as color contour plots in Figs. 7(b) and 7(c) with intrinsic broadening included. The Q-integrated results are also presented in Figs. 7(e) and 7(f). For Fig. 7(f), data simulated without intrinsic broadening is also included. At low signal levels, the measured data approaches a constant value, above the simulations. This indicates that there is a background contribution, limiting the measurement sensitivity, that is not captured in the Monte Carlo simulations, nor by the Al can subtraction. The additional background could arise from a combination of effects including imperfect Al background subtraction and multiple scattering involving the magnetic response or events partially external to the sample. There may also be a contribution from fission neutrons in the sample that moderate in the instrument shielding.

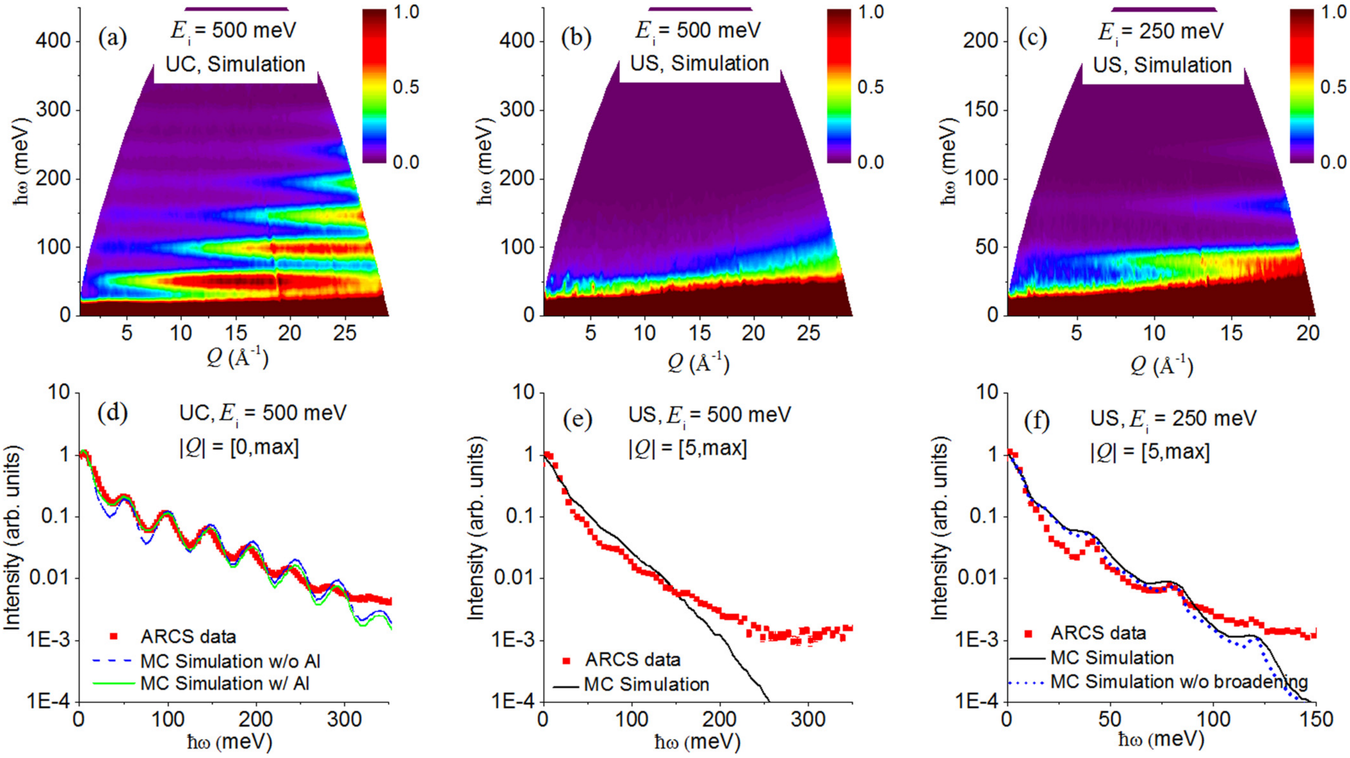

FIG. 7. Color contour plots from the Monte Carlo ray tracing simulations described in text are shown here for (a) UC, $E_i = 500$ meV, (b) US, $E_i = 500$ meV and (c) US, $E_i = 250$ meV. The simulations that incorporate intrinsic broadening of the QHO modes agree well with the data for UC, but not for the case of US. (d), (e), and (f) show the corresponding Q-integrated plots for the three experimental data sets, and compare them directly to the results from the simulations. Since an Al background subtraction was not performed for UC, simulations both including and excluding an Al contribution are shown in (d). Furthermore, the MC simulation results shown in (f) are presented for two different cases: (i) including and (ii) excluding intrinsic broadening of the QHO modes.

When comparing the high-energy vibrational modes of UC, UN, and US it is apparent that the differences in the U:X mass ratio (U:C = 19.8, U:N = 17, U:S = 7.4) lead to more obvious QHO behavior in the lighter atoms. As the U:X mass ratio decreases, the dispersion of the optic phonon modes has been shown to increase systematically [3], shifting the vibrational behavior of the light atoms further away from the localized QHO picture. A smaller U:X mass ratio has also the effect of pushing the optic phonon frequencies down closer in energy to the acoustic modes, so any resulting QHO excitations tend to be more closely spaced and therefore harder to resolve for a given instrumental energy resolution in neutron scattering experiments.

IV. ANHARMONICITY AND ANISOTROPY

In general, anharmonicity in lattice vibrations is manifested in the linewidths of phonon modes. On the other hand, anharmonic local potentials for the light atoms in the UX salts should result in unequal spacings of the oscillator levels, providing the possibility of complementary insight into the anharmonicity of the systems. There is also a possibility that an anisotropic local potential would result in different oscillator frequencies, and perhaps departures from harmonicity, in different directions. Experimental examples of these behaviors are given in metals with H in interstitial positions, see TaH [44] and ZrH_2 [45] for discussions on anharmonicity and anisotropy of the local potential for the H atoms, respectively.

The high-energy vibrational data presented to this point for both UC and UN [18] have been orientationally averaged, so only Q is considered and not **Q**. Clearly the QHO description of this data works very well, so overall the modes are highly isotropic. To see whether anisotropy and/or anharmonicity are experimentally observable in the QHO modes of UC, we collected a $E_i = 700$ meV data set with very high statistics along three crystallographic directions, [100], [110], and [111]. The C atoms have nearest neighbor distances along these directions in the ratio of $1{:}\sqrt{2}{:}\sqrt{3}$, as one can see from considering the crystal structure shown in Fig. 8(a). Unfortunately, both anharmonic and anisotropic features will be masked by the effect of multiple scattering, since at any value of Q it tends to cause peaks to appear at locations corresponding to $n\hbar\omega_0$. As a result, a straightforward plotting of oscillator peaks along different directions does not show evidence for either of these effects, and additional analysis is needed to account for the multiple scattering.

As an effort to minimize the effect of multiple scattering present in the single crystal data, we take advantage of the fact discussed earlier that the small Q scattering for the higher modes is totally dominated by multiple scattering, and use the low Q data as a pseudobackground. For each of the three directions, we integrate over a range perpendicular to that direction given by $|Q_\perp| = [-2,2]$ Å^{-1}. As a signal we use the

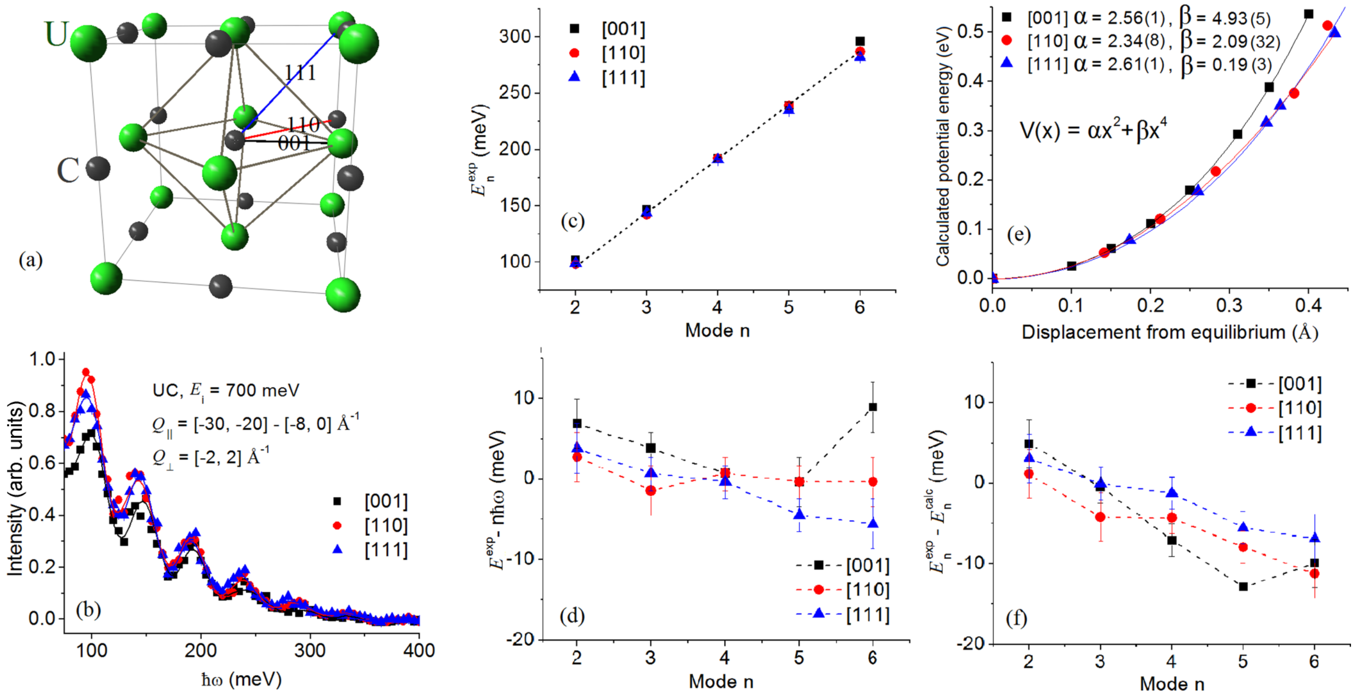

FIG. 8. (a) The crystal structure of the binary uranium systems UX. The light X atom is in an octahedral cage of U atoms. The colored lines indicate the three primary crystallographic directions, [001], [110], and [111]. The carbon atom nearest neighbor distances in these directions are in the ratio of $1{:}\sqrt{2}{:}\sqrt{3}$. (b) Constant-E difference cuts along the major crystallographic directions [001], [110], and [111] for UC. The solid curves are fits of the data to Eq. (5). (c) Peak positions along the three different directions taken from the fits in (b). The dotted line corresponds to the expected peak positions for an isotropic QHO. (d) The difference between the peak positions of the modes from our UC data and a perfectly harmonic potential. (e) Local potential of the carbon atoms calculated by DFT. The solid curves are fits to the anharmonic function $V(x)$ given in the text. (f) The difference between the peak positions of the UC data and the result from the DFT calculations.

high-Q part of the scattering defined by $20 < Q_\parallel < 30$ Å^{-1}, and as a background we utilize the region $0 < Q_\parallel < 8$ Å^{-1}. The subtraction of these two Q regions leads to constant-Q difference cuts along the three directions as shown in Fig. 8(b). Note that the $n = 1$ peak is not sufficiently resolved in the $E_i = 700$ meV data to be included here.

The difference cuts are fit to Eq. (5) to determine mode positions along the [001], [110], and [111] directions; fits are indicated in Fig. 8(b) by the solid curves, and the fitted peak positions are listed in Table V. These are also shown in Fig. 8(c), with the mode positions determined from the data ($E_n^{\rm exp}$) and the dashed curve representing the expectation for an ideal carbon QHO with $\hbar\omega_0 = 48 \pm 1$ meV. Figure 8(d) shows the difference between the mode positions for the ideal model ($n\hbar\omega_0$) and the experiment. The error bars are statistical and are larger than those for fits to the powder averaged data, presumably due to the lower number of counts in this single crystal data set. From the fits, the average oscillator energies are given for the different directions as $E_{001} = 49.0(6)$ meV, $E_{110} = 48.0(6)$ meV, and $E_{111} = 47.9(6)$ meV. There is no compelling evidence for anisotropy in the potential although the experimental data along the [001] direction exhibit systematically higher energies for the QHO modes than those along the other directions. This observation is compatible with density functional theory (DFT) calculations discussed below.

TABLE V. Peak positions of the QHO modes (in meV) extracted from fitting difference cuts of the $E_i = 700$ meV single-crystal UC data along three major crystallographic directions. The form of the difference cuts is explained in the text.

n	[001]	[110]	[111]
1	…	…	…
2	102(3)	98(3)	99(3)
3	147(2)	142(3)	144(3)
4	192(2)	192(2)	191(2)
5	239(3)	239(2)	235(2)
6	296(3)	287(2)	282(3)

To gain insight into any expected anisotropy and anharmonicity of the oscillator modes in UC, we have used DFT to calculate the potentials seen by the C atoms (see Appendix for details). The calculated potentials for the three principal directions are shown by the symbols in Fig. 8(e). The potential in each direction is described well by the following expression:

$$V(x) = \alpha x^2 + \beta x^4 \tag{10}$$

with the results shown by the solid lines in the figure. The values determined for α and β are also indicated. The calculation shows a small amount of anisotropy, and also indicates that the anharmonicity should be maximized along the [001] direction. The latter result suggests that the harmonic approximation begins to break down for the direction with the shortest nearest-neighbor distance. Indeed the fitted β for [001] is more than twice the magnitude of the β's along the other directions.

Assuming that the x^4 term is small, the energy levels corresponding to this potential can be calculated according to first-order perturbation theory [46], with the nth energy level corresponding to

$$E_n = \hbar\omega_0(n + 1/2) + \left(\frac{\hbar}{2m\omega_0}\right)^2 \beta(6n^2 + 6n + 3), \quad (11)$$

and the energy difference between the nth level and the $n = 0$ ground state given by

$$E_n - E_0 = n\hbar\omega_0 + 6\beta C^2(n^2 + n) \quad (12)$$

with $C = \hbar/2m\omega_0$.

Assuming that the first mode occurs at 48 meV, the energies of higher QHO levels along each of the three directions can be calculated using Eq. (12) along with each direction's corresponding α and β shown in Fig. 8(e). Figure 8(f) displays the difference between the oscillator mode positions determined from the experiment and the value E_n^{calc} from first-order perturbation theory. The downward slope indicates that the experimentally determined anharmonicity is not as large as the theoretical estimate. One must bear in mind that despite the attempt to correct for multiple scattering in the data, it makes up a larger fraction of the total signal at higher-order QHO peak positions. This multiple scattering can effectively mask subtle anharmonic effects.

V. CONCLUSIONS

For the binary crystal UC, time-of-flight neutron scattering measurements reveal a series of well-defined, equally spaced, high-energy vibrational modes that can be attributed to quantum harmonic oscillator behavior of the carbon atoms in this system. Measurements of the QHO modes along the high-symmetry [001], [110], and [111] directions reveal that these excitations are characterized by at most only a very small amount of anharmonicity and anisotropy. Similar time-of-flight neutron scattering data for US also shows evidence for the high-energy vibrational modes, but only a few are clearly observed and they are much weaker in intensity. The difference can be understood by considering the U:X mass ratio, the quantity b^2/m that characterizes the scattering strength of the modes, and the interference of Al recoil scattering with the QHO signal in US. Some progress has been made in modeling the various contributions to the scattering, but a better way to handle multiple scattering will be needed to accurately measure anharmonicity and anisotropy in the QHO modes.

Aside from the beautiful textbook physics the QHO modes represent, they may also have implications for other studies of the UX family. In particular, the exotic magnetic excitations of UN and US are now known to extend in energy above the optic phonon modes. Therefore the QHO modes need to be treated as background to isolate the magnetic scattering, which is an important step towards understanding its true origin. It is also interesting to consider whether the QHO modes are relevant to the possible use of UC and UN as next generation nuclear reactor fuels. The localized and strongly harmonic nature of the modes suggests that they will have little effect on the thermal conductivity of the materials, even at high temperatures. On the other hand, it is possible that the modes need to be properly accounted for to ensure sufficient accuracy in calculations of the total neutron scattering cross sections.

ACKNOWLEDGMENTS

We are grateful to P. De V. Duplessis for growth of the excellent sample. This research was supported by the Basic Energy Sciences, U.S. Department of Energy. A.A.A., G.E.G., D.L.A., M.B.S. and S.E.N. were fully supported and J.Y.Y.L was partially supported by the Scientific User Facilities Division. G.D.S. and G.M.S. were fully supported by the Materials Sciences and Engineering Division. Neutron scattering experiments were performed at the Spallation Neutron Source, which is sponsored by the Scientific User Facilities Division. Y.Y. was supported by Office of Experimental Program to Stimulate Competitive Research (Grant No. DE-FG02-08ER46528), Basic Energy Sciences, U.S. Department of Energy.

APPENDIX : DFT CALCULATIONS

For UC, the electronic structure within the density functional theory (DFT) was obtained using the Quantum ESPRESSO package [47] with a scalar relativistic approach. The calculation was performed using a plane-wave basis set and an ultrasoft pseudopotential [48] optimized in a RRKJ scheme [49]. The uranium pseudopotential was obtained from an ionized electronic configuration: $6p^6 6d^1 5f^3 7s^1$ with cutoff radii equal to 3.5 atomic units (a.u.), 1.7 a.u., 2.6 a.u. and 1.6 a.u. for s, p, d, and f angular momentum. The electronic levels deviate from the all-electron ones by less than 0.1 meV. We used the Perdew, Burke, Ernzerhof [50] exchange-correlation functional. The Brillouin zone (BZ) summations were carried out over a $4 \times 4 \times 4$ supercell. The electronic smearing with a width of 0.02 Ry was applied according to the Methfessel-Paxton method. The plane wave energy and charge density cutoffs were 73 and 1054 Ry, respectively, corresponding to a calculation accuracy of 0.2 mRy/atom. The carbon atom potential was obtained from the total energy modification of a $2 \times 2 \times 2$ supercell when one carbon atom was shifted from the equilibrium position in the [100], [110], or [111] directions and the remaining atoms were held fixed in their equilibrium positions.

---

[1] M. Kuznietz, G. H. Lander, and F. P. Campos, J. Phys. Chem. Solids **30**, 1642 (1969).

[2] F. A. Wedgwood, J. Phys. C: Solid State Phys. **5**, 2427 (1972).

[3] F. A. Wedgwood, J. Phys. C: Solid State Phys. **7**, 3203 (1974).

[4] W. J. L. Buyers, A. F. Murray, T. M. Holden, E. C. Svensson, P. de V. DuPlessis, G. H. Lander, and O. Vogt, Physica B **102**, 291 (1980).

[5] W. J. L. Buyers, A. F. Murray, J. A. Jackman, T. M. Holden, P. de V. DuPlessis and O. Vogt, J. Appl. Phys. **52**, 2222 (1981).

[6] T. M. Holden, W. J. L. Buyers, E. C. Svensson, and G. H. Lander, Phys. Rev. B **26**, 6227 (1982).

[7] T. M. Holden, W. J. L. Buyers, E. C. Svensson, J. A. Jackman, A. F. Murray, O. Vogt, and P. de V. DuPlessis, J. Appl. Phys. **53**, 1967 (1982).

[8] T. M. Holden, W. J. L. Buyers, E. C. Svensson, and G. H. Lander, Phys. Rev. B **30**, 114 (1984).

[9] W. J. L. Buyers, T. M. Holden, J. A. Jackman, A. F. Murray, P. de V. DuPlessis and O. Vogt, J.Mag. Mag. Mater. **31**, 229 (1983).

[10] J. A. Jackman, T. M. Holden, W. J. L. Buyers, P. de V. DuPlessis, O. Vogt, and J. Genossar, Phys. Rev. B **33**, 7144 (1986).

[11] T. M. Holden, J. A. Jackman, W. J. L. Buyers, K. M. Hughes, M. F. Collins, P. de V. DuPlessis, and O. Vogt, J. Mag. Mag. Mater. **63**, 155 (1987).

[12] K. M. Hughes, T. M. Holden, W. J. L. Buyers, P. de V. DuPlessis and M. F. Collins, J. Appl. Phys. **61**, 3412 (1987).

[13] N. A. Curry, Proc. Phys. Soc. **86**, 1193 (1965).

[14] E. F. Westrum, R. R. Walters, H. E. Flotow, and D. W. Osborne, J. Chem. Phys. **48**, 155 (1968).

[15] D. E. Burkes, R. S. Fielding, D. L. Porter, M. K. Meyer, and B. J. Makenas, J. Nucl. Mater. **393**, 1 (2009).

[16] Q. Yin, A. Kutepov, K. Haule, G. Kotliar, S. Y. Savrasov, and W. E. Pickett, Phys. Rev. B **84**, 195111 (2011).

[17] Z.-G. Mei, M. Stan, and B. Pichler, J. Nucl. Mater. **440**, 63 (2013).

[18] A. A. Aczel, G. E. Granroth, G. J. MacDougall, W. J. L. Buyers, D. L. Abernathy, G. D. Samolyuk, G. M. Stocks, and S. E. Nagler, Nat. Commun. **3**, 1124 (2012).

[19] G. Dolling, T. M. Holden, E. C. Svensson, W. J. L. Buyers, and G. H. Lander, *Phonons: Proceedings of the International Conference on Lattice Dynamics, Paris, 5-7 Sept. 1977*, edited by M. Balkanski (Flammarion, Paris, 1978), p. 81.

[20] G. E. Granroth, D. H. Vandergriff, and S. E. Nagler, Physica B **385**, 1104 (2006).

[21] G. E. Granroth, A. I. Kolesnikov, T. E. Sherline, J. P. Clancy, K. A. Ross, J. P. C. Ruff, B. D. Gaulin, and S. E. Nagler, J. Phys.: Conf. Ser. **251**, 012058 (2010).

[22] D. L. Abernathy, M. B. Stone, M. J. Loguillo, M. S. Lucas, O. Delaire, X. Tang, J. Y. Y. Lin, and B. Fultz, Rev. Sci. Instrum. **83**, 015114 (2012).

[23] J. Y. Y. Lin, A. A. Aczel, D. L. Abernathy, S. E. Nagler, W. J. L. Buyers, and G. E. Granroth, Phys. Rev. B **89**, 144302 (2014).

[24] M. Warner, S. W. Lovesey, and J. Smith, Z. Phys. B **51**, 109 (1983).

[25] M. T. Dove, *Introduction to Lattice Dynamics* (Cambridge University Press, Cambridge, 1993).

[26] S. Ikeda and N. Watanabe, J. Phys. Soc. Jpn. **56**, 565 (1987).

[27] A. I. Kolesnikov, I. O. Bashkin, V. Yu. Malyshev, E. G. Ponyatovsky, M. Prager, and J. Tomkinson, Physica B **180**, 284 (1992).

[28] A. I. Kolesnikov, I. O. Bashkin, A. V. Belushkin, E. G. Ponyatovsky, and M. Prager, J. Phys.: Cond. Matt. **6**, 8989 (1994).

[29] C. Elsässer, K. M. Ho, C. T. Chan, and M. Fähnle, Phys. Rev. B **44**, 10377 (1991).

[30] R. Caputo, A. Alavi, Mol. Phys., **101**, 1781 (2003).

[31] H. G. Smith and W. Glaser, *Phonons: Proceedings of the International Conference, Rennes, France 1971*, edited by M. A. Nusimovici (Flammarion, Paris, 1971), p. 145.

[32] P. de V. DuPlessis, T. M. Holden, W. J. L. Buyers, J. A. Jackman, A. F. Murray, and C. F. Van Doorn, J. Phys. C **18**, 2809 (1985).

[33] G. Peckham, Proc. Phys. Soc. **90**, 657 (1967).

[34] V. F. Sears, Neutron News, **3**, 26 (1992).

[35] S. E. Nagler, D. A. Tennant, R. A. Cowley, T. G. Perring, and S. K. Satija, Phys. Rev. B **44**, 12361 (1991).

[36] Toby Perring, Ph.D. thesis, Cambridge University, 1989.

[37] J. Y. Y. Lin, H. L. Smith, G. E. Granroth, D. L. Abernathy, M. D. Lumsden, B. Winn, A. A. Aczel, M. Aivazis, and B. Fultz, Nuclear Inst. and Methods in Physics Research A **810**, 86 (2016).

[38] E. Farhi, C. Monzat, R. Arnerin, T. van Vuure, C. Castén-Guerrero, C. Hennane, P. A. Harraud, G. Campioni, S. Fuard, J. Ollivier and P. Willendrup, J. Neutron Res. **17**, 63 (2014).

[39] B. Fultz *et al.*, DANSE: Distributed data analysis for neutron scattering experiments, http://danse.us.

[40] K. Lefmann and K. Nielsen, Neutron News **10**, 20 (1999).

[41] P. Willendrup, E. Farhi, and K. Lefmann, Physica B **350**, E735 (2004).

[42] G. E. Granroth and D. L. Abernathy, Proceedings of ICANS-XVI, 289 (2003).

[43] G. E. Granroth, M. Chen, J. A. Kohl, M. E. Hagen and J. W. Cobb, J. Neutron Res. **15**, 91 (2007).

[44] R. Hempelmann and D. Richter, and A. Kollmar, Z. Phys. B **44**, 159 (1981).

[45] J. G. Couch, O. K. Harling, and L. C. Clune, Phys. Rev. B **4**, 2675 (1971).

[46] David J. Griffiths, *Introduction to Quantum Mechanics*, 2nd ed. (Pearson Prentice Hall, Englewood Cliffs, NJ, 2004).

[47] P. Giannozzi *et al.*, J. Phys.: Cond. Matt. **21**, 395502 (2009).

[48] D. Vanderbilt, Phys. Rev. B **41**, 7892 (1990).

[49] A. M. Rappe, K. M. Rabe, E. Kaxiras, and J. D. Joannopoulos, Phys. Rev. B **41**, 1227 (1990).

[50] J. P. Perdew, K. Burke, and M. Ernzerhof, Phys. Rev. Lett. **77**, 3865 (1996).